applied optics

Self-calibration for lensless color microscopy

Olivier Flasseur,[1,*] Corinne Fournier,[1] Nicolas Verrier,[2] Loïc Denis,[1] Frédéric Jolivet,[1] Anthony Cazier,[1] and Thierry Lépine[1]

[1]Université de Lyon, UJM-Saint-Etienne, CNRS, Institut d'Optique Graduate School, Laboratoire Hubert Curien UMR 5516, 18 rue Professeur Benoit Lauras, F-42000 Saint-Etienne, France
[2]Université de Haute-Alsace, Laboratoire MIPS, EA 2332, 61 rue Albert Camus, F-68200 Mulhouse, France
*Corresponding author: olivier.flasseur@univ-st-etienne.fr

Received 5 December 2016; revised 16 February 2017; accepted 23 February 2017; posted 1 March 2017 (Doc. ID 281955); published 7 April 2017

Lensless color microscopy (also called in-line digital color holography) is a recent quantitative 3D imaging method used in several areas including biomedical imaging and microfluidics. By targeting cost-effective and compact designs, the wavelength of the low-end sources used is known only imprecisely, in particular because of their dependence on temperature and power supply voltage. This imprecision is the source of biases during the reconstruction step. An additional source of error is the crosstalk phenomenon, i.e., the mixture in color sensors of signals originating from different color channels. We propose to use a parametric inverse problem approach to achieve self-calibration of a digital color holographic setup. This process provides an estimation of the central wavelengths and crosstalk. We show that taking the crosstalk phenomenon into account in the reconstruction step improves its accuracy.

OCIS codes: (090.1995) Digital holography; (090.1705) Color holography; (100.3190) Inverse problems; (150.1488) Calibration; (100.3010) Image reconstruction techniques.

https://doi.org/10.1364/AO.56.00F189

1. INTRODUCTION

Lensless microscopy is an established method to locate and estimate the size of micrometric objects in a volume [1,2]. This technique is used in many areas including study of fluid flows [3,4] and biomedical imaging [5,6]. Its main advantages are its robustness, simplicity and low-cost implementation. Its main limitations are well known and inverse problem approaches can push back some of these limits [7,8]. Lensless color microscopy applies to imaging of colored 3D and/or dephasing objects [9].

The use of CMOS sensors equipped with a Bayer filter and of LED or laser diodes makes it possible to obtain compact and cost-effective setups. However, uncertainty about the actual wavelengths of the laser sources may be a source of error during the holographic reconstruction step. In addition, the crosstalk phenomenon causes a mixture between the signals received on each channel.

In Section 2, we describe the principle of lensless color microscopy and detail the possible causes and consequences of its incorrect calibration in the context of cost-effective setups. In Section 3, we describe a self-calibration method based on a reconstruction algorithm that uses a parametric inverse problem approach. In Section 4, we present a fast, simple and cost-effective experimental method to estimate the laser diode wavelengths and the mixing matrix of the crosstalk. Finally, in Section 5, we discuss and compare the theoretical precision limits of monochromatic and color holography.

2. LENSLESS COLOR MICROSCOPY AND ITS CALIBRATION ISSUES

A. Lensless Color Microscopy

The holographic setup used in this study is an in-line and lensless setup, as originally proposed by Dennis Gabor [10,11], with a digital color sensor and three coherent lasers for illumination. The waves diffracted by the objects under study are recorded by the sensor. Figure 1 shows a schematic representation of the experimental setup.

We will illustrate our self-calibration method on our experimental setup in which three laser diodes are used, one red (Thorlabs, CPS635R, 1.5 mW), one green (Thorlabs, CPS532, 4.5 mW) and one blue (Thorlabs, CPS405, 4.5 mW). Their nominal wavelengths provided by the manufacturer are, respectively, $\lambda_R^{\text{nom}} = 635$ nm, $\lambda_G^{\text{nom}} = 532$ nm and $\lambda_B^{\text{nom}} = 405$ nm. The holograms are recorded by a 12-bit CMOS sensor (Basler, daA2500-14uc) with $A \times B = 1944 \times 2592$ pixels with a 2.2 μm pitch.

The conventional approach to reconstructing a hologram is based on simulations of hologram diffraction by backpropagation [12,13]. However, the reconstructed planes are affected by many artifacts (edge effects, twin images, presence of

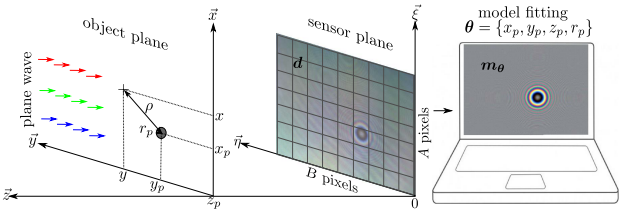

Fig. 1. Lensless color microscopy setup.

out-of-focus objects, etc.). In contrast, reconstructions based on an inverse problem approach [14,15] are significantly improved. These reconstructions are obtained by maximizing the likelihood between a model of the object diffraction pattern and the recorded data (the hologram), and possibly by including regularization terms [16,17]. We describe the principle of these methods in more details in Section 3.

B. Calibration Issues of Lensless Color Microscopy

To ensure compactness and cost-effectiveness, the sources used are often laser diodes. Similarly, the color sensor used is often a single sensor equipped with a Bayer filter. In this section, we describe the possible sources of error during the reconstruction step in lensless color microscopy. The consequences of badly calibrated parameters are similar whether the reconstruction is performed with a conventional approach (light backpropagation simulation) or with an inverse problem approach.

1. Calibration Issues Related to the Wavelengths of the Sources

To perform reconstruction from color holograms, an accurate knowledge of the wavelengths of the laser sources is mandatory. Indeed, whatever the reconstruction approach, the propagation kernel used in classical reconstruction approaches and the image formation model used in inverse problems both depend on the wavelength. In monochromatic holography and under Fresnel assumption, an error on the wavelength leads to an error on the depth of the maximum-of-focus reconstruction. In color lensless microscopy, errors on the wavelengths lead to a non-unique focus plane.

The present study is also justified by the development and massive use of inexpensive lasers, which represent a good trade-off between cost and performance compared with the high-end lasers commonly used in lensless microscopy. However, low-cost lasers do not necessarily deliver light at a wavelength equal to the nominal value provided by the manufacturer [18]. Wavelengths can also change during the experiment due to the heating of the lasers or variations of the power level if no control is enforced on these parameters. Table 1 shows the ranges of wavelengths provided by the manufacturer for the three laser diodes that we use, within the temperature and power operating ranges provided by the manufacturer.

Table 1. Ranges of Wavelengths of the Laser Sources (CPS635R, CPS532, and CPS405), Provided by Thorlabs

	$\lambda^{\min}$ (nm)	λ^{nom} (nm)	$\lambda^{\max}$ (nm)	T (°C)	Power (mW)
Red	630	635	645	−10/50	1.0/1.4
Green	531	532	533	10/40	4.0/5.0
Blue	400	405	410	−10/40	4.0/5.0

In the following, the line vector $\boldsymbol{\lambda} = (\lambda_R, \lambda_G, \lambda_B)$ designates the wavelengths of each of the three sources, while the optional exponent indicates the set of wavelengths considered [for example, $\boldsymbol{\lambda}^{\text{nom}} = (\lambda_R^{\text{nom}}, \lambda_G^{\text{nom}}, \lambda_B^{\text{nom}})$ for the nominal wavelengths].

Conventionally, when estimating the object depth z_p (i.e., the distance from the object to the sensor), the source wavelength λ is kept fixed. However, under Fresnel assumption, the Fresnel free-space propagator $h(x, y)$ depends on the product λz_p: $h(x, y) \propto \exp[j\pi(x^2 + y^2)/(\lambda z_p)]$ (see [12]). As a result, the imprecision Δ_{z_p} on the estimated value z_p is related to the imprecision Δ_λ on the wavelength λ of the source through

$$\frac{\Delta_\lambda}{\lambda} = \frac{\Delta_{z_p}}{z_p}. \tag{1}$$

According to Eq. (1) and the uncertainties on the wavelengths listed in Table 1, the maximum bias $\Delta_{z_p}^{\max}$ on the estimated parameter z_p can reach 1 mm for an object located 7 cm from the sensor plane. This error appears to be prohibitive for any metrological application. Thus, it appears that if the real wavelengths $\boldsymbol{\lambda}^{\text{real}} = (\lambda_R^{\text{real}}, \lambda_G^{\text{real}}, \lambda_B^{\text{real}})$ that contributed to the hologram formation differ from the wavelengths used within the diffraction model, three different depths will be estimated for the same opaque object. The three estimated values $\{z_R^{\text{est}}, z_G^{\text{est}}, z_B^{\text{est}}\}$ of the z_p distance obtained from three holograms recorded with wavelengths $\boldsymbol{\lambda}^{\text{real}}$ and reconstructed assuming wavelengths $\boldsymbol{\lambda}^{\text{nom}}$ satisfy the following system of equations:

$$\begin{cases} \lambda_R^{\text{nom}} \cdot z_R^{\text{est}} = \lambda_R^{\text{real}} \cdot z_p, \\ \lambda_G^{\text{nom}} \cdot z_G^{\text{est}} = \lambda_G^{\text{real}} \cdot z_p, \\ \lambda_B^{\text{nom}} \cdot z_B^{\text{est}} = \lambda_B^{\text{real}} \cdot z_p. \end{cases} \tag{2}$$

Rather than using the nominal values provided by the manufacturer, these wavelengths should be calibrated, using either a spectrometer during a calibration step, or a self-calibration approach, as described in Section 2.B.

2. Calibration Issues Related to the CMOS Color Sensor

From a cost-effective perspective, color sensors using CMOS technology and a Bayer filter are a preferred choice. In this section, we describe the different crosstalk phenomena, which occur on this type of sensors as well as their possible consequences during the holographic reconstruction.

The term "crosstalk" refers to the undesirable effects that occur when a signal transmitted on a channel modifies or impacts the signals transmitted on the other channels. This global phenomenon leads to a reduction in sensitivity, poor separation of colors and a degradation of spatial and frequency resolution. The main crosstalk phenomena appearing on color sensors are spectral, optical and electronic [19–21]. We provide below a brief description of each of these phenomena, focusing on how to quantify and reduce them.

Spectral crosstalk: CMOS sensors classically used in a cost-effective lensless color microscopy scheme often do not allow trichromatic information to be obtained at each photodetector [22,23]. Consequently, the photodetectors are covered by a

matrix of chromatic filters called "Bayer color filter array" [24], which filters the incident light by transmitting only one of the three primary components at each pixel. This step, called "mosaicking", is mandatory to record color images with this type of sensor, since the photodetectors used are sensitive to incident wave intensity over a wide spectral range. Spectral crosstalk is due to the Bayer filter covering the photodetector layer of the CMOS color sensors: their spectral responses are not ideal bandpass [25]. Figure 2 shows the spectral responses as a function of wavelength for the filters of the Basler daA2500-14uc camera. A significant overlap between the different spectral responses can be noted.

In 2002, Yamaguchi *et al.*, presented one of the first uses of digital sensors equipped with a Bayer filter for a color holography application [26]. Spectral crosstalk was mentioned in the sensor spectral responses, but its characterization was not addressed. It should also be noted that a simple average of the light intensity received on each channel during a monochromatic exposure does not provide an accurate estimate of the spectral crosstalk. Indeed, the electrical signal produced by a low-cost camera is not exactly linearly related to the intensity of the optical signal on the sensor (for example, an offset may be present). In addition, time-varying fringes can be observed on the hologram backgrounds obtained with low-cost cameras. These fringes may be produced by a parallelism defect of the fine glass slides that protect the detector. This phenomenon makes it difficult to characterize the spectral crosstalk since the number of dark fringes does not remain constant during the recording, whereas the spectral crosstalk phenomenon remains constant. As a consequence, the establishment of the spectral responses of the Bayer filters remains the gold standard method for quantitatively studying the spectral crosstalk phenomenon. For example, Ozcan's group at UCLA has recently proposed using a setup composed of a broadband laser source coupled to an acousto-optical filter that can be adjusted in wavelength around a fine bandwidth in order to accurately measure the spectral response of the filters [27].

In order to reduce the influence of spectral crosstalk, it is possible to use more selective pigments to stain Bayer filters such as those developed by Micron Technologies, Aptina. It is also possible to reduce the visual degradation induced by spectral crosstalk with additional numerical post-treatments and/or with a configuration of the color filter array different from that proposed by Bayer [28,29]. However, in digital holography, low-pass filtering induced by de-mosaicking attenuates the high frequencies and, thus, blurs the reconstruction. In addition, it has been recently proposed to replace the traditional color filter array with a plasmonic color filter directly lithographed close to the photodetectors [30–32]. This method has the advantage of simultaneously reducing the spectral and optical crosstalk while increasing the transmission of the filters. This method is not yet applicable in a low-cost scheme, though.

In Section 4, we propose a method for estimating the signal mixing induced by this crosstalk phenomenon and to take it into account for applications in lensless color microscopy.

Optical crosstalk: Optical crosstalk occurs when the incident angle becomes too large for the microlens array to focus light on the photodetector immediately below. In this case, a portion of the signal of interest may be lost in the gap that separates two adjacent photodetectors or, worse, may impact a neighboring photodetector. Figure 3 illustrates this phenomenon. No optical crosstalk occurs at null or weak incidence angles [cases **(b)** ① and **(b)** ②]. At higher incidence angles [case **(b)** ③], optical crosstalk can occur.

Since it is difficult to study this effect without taking into account the influence of other crosstalk phenomena, its importance is mainly determined by numerical simulations [33]. Since the incidence angles of the light beams striking the pixels

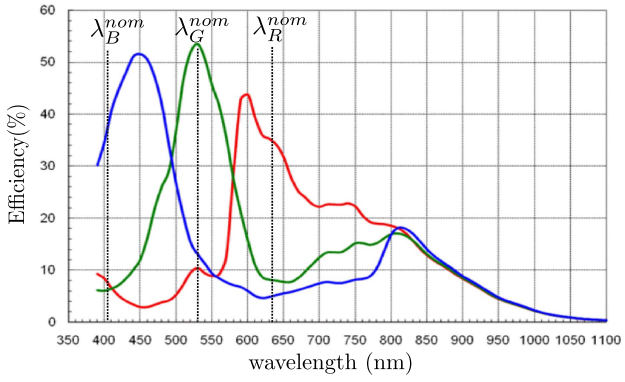

Fig. 2. Spectral responses of Bayer filter (according to Basler, daA2500-14uc).

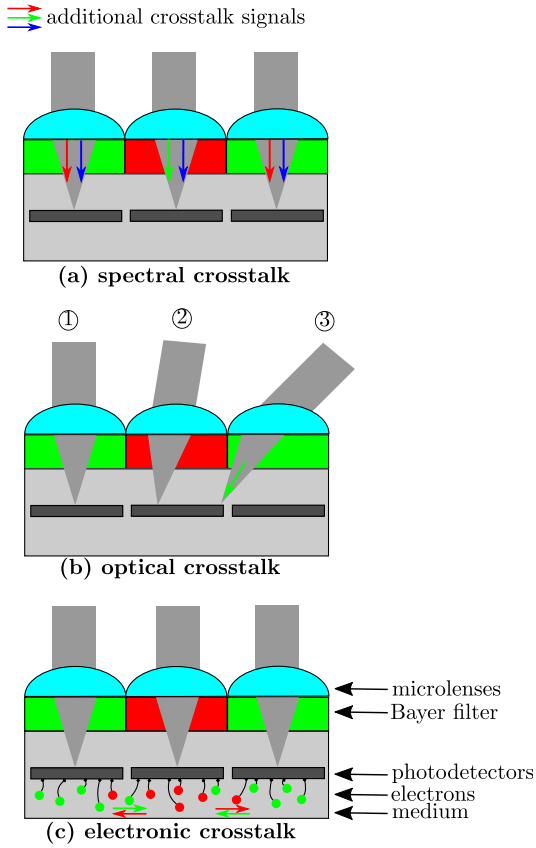

Fig. 3. Illustration of (a) spectral, (b) optical, and (c) electronic crosstalk phenomena.

Table 2. Spectral, Optical and Electronic Crosstalk Characteristics

Crosstalk	Spectral	Optical	Electronic
Cause	Bayer filters	Microlenses	Electrons leakage
Classical method of quantification	Bayer filter responses	Numerical simulations	S-cube system
Classical methods of reduction	Filter improvement, Post-treatments	Microlens position, Photodetector treatment	Waveguide, Deep substrate

located at the edge of the sensor are naturally higher than those of the beams on the central part of the sensor, it is possible to optimize the placement of the microlenses with respect to the Bayer filters (by slightly shifting their center), in order to favor the convergence of the rays on the photodetectors of interest and thus reduce the optical crosstalk [33]. It is also possible to apply surface treatments (antireflective, etc.) to the surface of the photodetectors [34].

In lensless microscopy, local optical crosstalk can be disregarded since the laser is collimated and, thus, the incidence angles of the light beams on the sensor are small (less than 2°).

Electronic crosstalk: Electronic crosstalk occurs due to an interaction between signals received at two neighboring photodetectors. Some electrons created as a result of detection of light in the depletion zone are diffused to adjacent photodetectors. This results in an additional error in the signal of interest as illustrated in Fig. 3 [case **(c)**].

This phenomenon is commonly quantified by the use of an S-cube system to illuminate a single pixel (at normal incidence) and, thus, measure the proportion of signal leaking to the neighboring pixels due to the electronic crosstalk effect [20].

Since the advent of CMOS sensors, many improvements and optimizations of the architecture have been made by foundries to limit the effects of electronic crosstalk. It can be considerably reduced by adding an insulating cage around neighboring photodetectors, which acts as a waveguide [34–37]. This technique also reduces the optical crosstalk [37]. It is also possible to increase the depth of the substrate [34]. The possible effects of this phenomenon are also taken into account in the overall crosstalk estimation scheme presented in Section 4.

Table 2 summarizes the causes and the conventional means of estimating and correcting various crosstalk phenomena.

Section 4 demonstrates that an inaccuracy on the wavelengths of low-cost laser diodes as well as the crosstalk phenomenon can significantly degrade the performance of the holographic reconstruction. In Section 4, we propose a simple, fast and cost-effective experimental method to reduce the uncertainty on the wavelength of the sources and to characterize the crosstalk phenomenon.

3. RECONSTRUCTION USING A PARAMETRIC INVERSE PROBLEM APPROACH

Based on an adequate image formation model, parametric inverse problem approaches provide accurate reconstructions that are "optimal" from a signal processing point of view, under an additive white Gaussian noise hypothesis. They have been successfully used for metrological applications [14,38–40] and appear to be the best methods to calibrate a monochromatic holographic setup [41]. We propose using such an approach to reconstruct a spherical opaque object and, thus, obtain an accurate calibration of the setup (i.e., low standard deviation and bias). The proposed method can be considered cost-effective as it only requires an opaque sphere in addition to the lensless color microscope.

The basics and mathematical formulation of this technique are described below. We consider an opaque sphere characterized by the parameter vector $\boldsymbol{\theta} = \{x_p, y_p, z_p, r_p\}$ in which $\{x_p, y_p\}$ represent the longitudinal coordinates in the object plane, z_p is the depth coordinate and r_p is the radius of the particle (see Fig. 1).

The intensity diffracted by the object and recorded at the $\{x, y\}$ position in the sensor plane on channel c ($c \in \{R = 1, G = 2, B = 3\}$) is

$$m^c_{\boldsymbol{\theta}}(x, y) = m^c_0 - \alpha^c_{\lambda(c)} \cdot g_{\lambda(c),\boldsymbol{\theta}}(x, y), \tag{3}$$

in which m^c_0 is an offset representing the intensity of the illumination wave, $\alpha^c_{\lambda(c)}$ is the amplitude factor of the interference pattern and $g_{\lambda(c),\boldsymbol{\theta}}$ represents the analytical model of the diffraction pattern for the object characterized by the parameters set $\boldsymbol{\theta}$ and illuminated by a plane wave at wavelength $\boldsymbol{\lambda}(c)$.

Since the opaque sphere is illuminated by a collimated coherent source and z_p is chosen so that $z_p \gg \frac{4\pi \cdot r_p^2}{\lambda(3)}$, $g_{\lambda(c),\boldsymbol{\theta}}$ can be described by a simplified Thompson's model [42] in which the second-order interference terms are neglected:

$$g_{\lambda(c),\boldsymbol{\theta}}(x, y) = \frac{r_p}{2 \cdot \rho(x, y)} J_1\left(\frac{2\pi \cdot r_p \cdot \rho(x, y)}{\boldsymbol{\lambda}(c) \cdot z_p}\right) \cdot \sin\left(\frac{\pi . \rho(x, y)^2}{\boldsymbol{\lambda}(c) \cdot z_p}\right), \tag{4}$$

where $\rho(x, y) = \sqrt{(x - x_p)^2 + (x - y_p)^2}$ and J_1 is the first-order Bessel function of the first kind.

Therefore, the color hologram model $\boldsymbol{m_\theta}(x, y)$ at position (x, y) on the sensor plane is the vector given in Eq. (5) in which each component is associated with one of the three sensor channels c:

$$\boldsymbol{m_\theta}(x, y) = \begin{pmatrix} m^R_{\boldsymbol{\theta}}(x, y) \\ m^G_{\boldsymbol{\theta}}(x, y) \\ m^B_{\boldsymbol{\theta}}(x, y) \end{pmatrix}. \tag{5}$$

The inverse approach consists of finding the best set of parameters $\boldsymbol{\theta}$ from the recorded color hologram $\boldsymbol{d}$, i.e., the set $\boldsymbol{\theta}$ that minimizes, in the least-square sense, the distance to the data:

$$\mathcal{C}(\boldsymbol{\theta}) = \sum_{c=1}^{3} \sum_{a=1}^{A} \sum_{b=1}^{B} w^c(a, b) \cdot (d^c(a, b) - m^c_{\boldsymbol{\theta}}(a, b))^2 \tag{6}$$

in which w^c is a binary weighting matrix of size $A \times B$ taking into account the Bayer mask (w^c is equal to 0 for 75% of the red and blue channels and for 50% of the green channel as shown in Fig. 4) and any defective pixel on channel c. More generally, $w^c(a, b)$ stands for the inverse of the noise variance at pixel

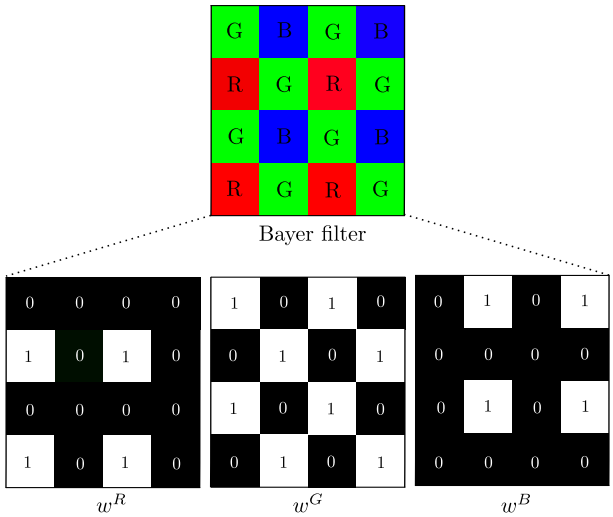

Fig. 4. Bayer filter and weighting matrices w^c for each color channel.

(a, b) on channel c [43]. The estimation process is performed jointly on the three channels ($c \in \{R = 1, G = 2, B = 3\}$).

4. SELF-CALIBRATION METHOD FOR A LENSLESS COLOR MICROSCOPY SETUP

The self-calibration process described hereafter has several advantages. First of all, it can be considered a cost-effective method as it only requires a spherical and calibrated opaque object. It is also simple to implement and fast. The overall process takes less than 4 min to obtain one estimate of wavelengths and 5 min to obtain one estimate of the crosstalk (on Intel i7-4800MQ, clock rate = 2.70 GHz) which seems reasonable in comparison with an experimental measurement of these parameters.

In order to study the proposed calibration method, we used a chrome-deposited opaque object behaving as an opaque sphere whose radius was 15 μm (Optimask, diameter ±1 μm, roundness error ±0.25 μm). It should be noted that, in practice, any spherical opaque object satisfying the Thompson model [42] can be used.

A. Estimation of the Wavelengths of the Sources

It is clear from Eq. (2) that it is impossible to jointly estimate the three wavelength values as well as the z_p parameter (underdetermined system). It is, thus, necessary to select one of the wavelengths as a reference that will not be estimated. In practice, the laser source with the smallest uncertainty is chosen. As a result, in the following, it is assumed that λ_G^{real} is equal to λ_G^{nom} since the green laser wavelength used has the smallest manufacturer uncertainty (±1 μm).

1. Principle of Wavelength Estimation Using the Parametric Inverse Approach

The method to estimate the wavelengths can be broken down into four steps.

Step ①: *Acquisition of three monochromatic holograms* at wavelengths $\boldsymbol{\lambda}^{\text{real}}$ that have to be estimated.

Step ②: *Independent reconstruction of each hologram* using the inverse parametric approach with nominal wavelength values $\boldsymbol{\lambda}^{\text{nom}}$ (no prior on the real wavelength values). Thus, at the end of this step, estimated parameters $\{x^{\text{est}}_{\{R,G,B\}}, y^{\text{est}}_{\{R,G,B\}}, z^{\text{est}}_{\{R,G,B\}}, r^{\text{est}}_{\{R,G,B\}}\}$ are obtained.

Step ③: *First estimation of the wavelengths of the sources*. From the hypothesis that λ_G^{real} equals λ_G^{nom}, it can be deduced that z_G^{est} and r_G^{est} are, respectively, the best estimation of z_p and r_p in the current step. From Eqs. (1) and (2), a first estimated wavelength of the red and blue sources is given by

$$\begin{cases} \lambda_R^{\text{est}_1} = \lambda_R^{\text{nom}} + \Delta_{\lambda_R} = \lambda_R^{\text{nom}} + \lambda_R^{\text{nom}} \cdot \frac{z_G^{\text{est}} - z_R^{\text{est}}}{z_G^{\text{est}}} \\ \lambda_B^{\text{est}_1} = \lambda_B^{\text{nom}} + \Delta_{\lambda_B} = \lambda_B^{\text{nom}} + \lambda_B^{\text{nom}} \cdot \frac{z_G^{\text{est}} - z_B^{\text{est}}}{z_G^{\text{est}}} \end{cases}. \quad (7)$$

Step ④: *Refinement of the red and blue wavelengths*. This estimation is carried out using an inverse problem approach in which the parameters z_p and r_p are jointly estimated. The transversal coordinates (x_p, y_p) and the red and blue wavelengths are also estimated. The estimation process is initialized to the most accurate parameter values available at this step – $\{x^{\text{est}}_{\{R,G,B\}}, y^{\text{est}}_{\{R,G,B\}}, z_G^{\text{est}}, r_G^{\text{est}}\}$ and $(\lambda_R^{\text{est}_1}, \lambda_G^{\text{nom}}, \lambda_B^{\text{est}_1})$. At the end of this step, a second estimated wavelength $(\lambda_R^{\text{est}_2}, \lambda_G^{\text{nom}}, \lambda_B^{\text{est}_2})$ of the sources is obtained.

It is important to note that **Step** ③ is a first estimate to be refined in **Step** ④. By initializing **Step** ④ to the estimated parameters closer to the real parameters than those available in **Step** ②, the computation time of **Step** ④ is reduced. It also reduces the risk of converging to a local minimum of the cost function given in Eq. (6).

2. Experimental Results and Discussion

This method was applied to a set of 65 experimental holograms ($z_p \simeq 7$ cm, $r_p = 15$ μm transversely shifted by a few pixels from each other) and compared with measured wavelengths using a high-resolution spectrometer (OceanOptics, QE65000) calibrated with a mercury spectral lamp (Philips, 93136E). A second-order polynomial interpolation is applied to reduce the measurement inaccuracy of the spectrometer from 0.8 nm to 0.3 nm on the central wavelength of the laser. Table 3 lists the mean value and standard deviation of the estimated wavelengths $\{\lambda_R^{\text{est}_2}, \lambda_B^{\text{est}_2}\}$ (lines 1 and 3) as well as the measured wavelengths (line 2). Line 1 gives the estimates if the green wavelength is set at its nominal value λ_G^{nom} (no prior on the wavelengths), while line 3 gives the estimates if the green wavelength is set at the wavelength λ_G^{meas} measured using a high-resolution spectrometer.

Within our experimental framework, it appears that the hypothesis assimilating the real green wavelength to its nominal value results in an overestimation of 0.6 nm. By considering Eq. (1) and a unique z for the three wavelengths, this bias

Table 3. Estimated and Measured Wavelengths of the Sources

	λ_R (nm)	λ_G (nm)	λ_B (nm)
Estimation ($\lambda_G^{\text{ref}} = \lambda_G^{\text{nom}}$)	638.3 ± 0.2	532 (ref.)	403.3 ± 0.2
Spectrometer	637.8 ± 0.3	531.4 ± 0.3	402.9 ± 0.3
Estimation ($\lambda_G^{\text{ref}} = \lambda_G^{\text{meas}}$)	637.6 ± 0.2	531.4 (ref.)	402.8 ± 0.2

generates a theoretical overvaluation of 0.7 nm for the red wavelength as well as a theoretical overvaluation of 0.5 nm for the blue wavelength. This is in agreement with the measured wavelengths of the sources obtained experimentally.

This method is constrained by the hypothesis assuming one of the three wavelengths to its nominal value. The uncertainty on the estimated wavelengths (for the two other sources) will increase with an increase in the manufacturer's uncertainty range on the wavelength chosen as reference. In this experiment, this hypothesis generates an uncertainty of ± 1 nm on the wavelength value of this source. This leads to an uncertainty of ± 1.2 nm on the estimated red wavelength $\lambda_R^{\text{est}_2}$ and an uncertainty of ± 0.8 nm on the estimated blue wavelength $\lambda_B^{\text{est}_2}$. Thus, using this estimation process reduces the uncertainty on the range of wavelength from 15 nm to $1.2 \times 2 = 2.4$ nm for the red source. Similarly, the uncertainty on the range of wavelength has been reduced from 10 nm to $0.8 \times 2 = 1.6$ nm for the blue source. It is thus shown by Table 3 line 3 that the absence of error in the hypothesis assimilating λ_G^{real} to λ_G^{nom} leads to a very accurate estimation of the two other wavelengths.

Moreover, beyond the relative precision of the estimation, it should also be noted that the deviations between the different estimated wavelengths are equal to the deviations between the different measured wavelengths. This point again emphasizes the interest of this method of estimation to improve the quality of the reconstructions. The limit of the method is reached when the uncertainties on the range of wavelength associated to each source provided by the manufacturer are similar. In that case, there is no gain in applying this method.

The proposed method is limited to estimating the central wavelength of the sources, while in practice, the sources are not monochromatic ones. In our setup, according to Thorlabs CPS635R and CPS405 datasheets, a temperature variation may also result in a slight change in the shape of the laser emission spectrum. In the literature, the effects of the spectral width of the light source on the hologram formation have been studied. It is thus shown that a non-monochromatic source generates a low-pass filtering of the propagation impulse response by a super-Gaussian function depending on the spectral width of the source [44,45]. This low-pass filtering effect will be added to the low-pass filtering due to the pixel integration. It should be possible to estimate this global low-pass filtering. Nevertheless, it appears that the spectral width is less crucial than the central wavelength of the sources. Indeed, not taking into account the spectral width in the image formation model [Eqs. (3) and (4)] leads to low residuals ($\boldsymbol{d} - \boldsymbol{m}_{\boldsymbol{\theta}}$) comparable to an additive white and Gaussian noise, proving a good agreement between the direct model we use and the experimental data.

B. Calibration of the Crosstalk Phenomenon Affecting the Sensor

As detailed in Section 2, the optical crosstalk, which is spatially dependent, can be neglected in lensless microscopy. In the following, we do not attempt to separate the contribution of the spectral crosstalk with respect to the electronic crosstalk, but rather obtain an estimate of the overall crosstalk, which can be included in the hologram formation model in order to improve the quality of the holographic reconstructions.

As a result, the proposed self-calibration method consists of determining a unique set of coefficients modeling the mixture of the signals received on each channel due to both the spectral and electronic crosstalks.

1. Principle of Crosstalk Estimation Using the Parametric Inverse Approach

A simple experimental method based on an inverse parametric approach is proposed to determine the mixing coefficients between the different color channels for a fixed wavelength set. In the presence of crosstalk, Eq. (3), which models the intensity diffracted on channel c, should be replaced with Eq. (8), which takes into account the mixture of signals coming from the different channels:

$$m_{\boldsymbol{\theta}}^{c}(x,y) = m_0^{c*} - \sum_{\ell=1}^{3} \alpha_{\boldsymbol{\lambda}(\ell)}^{c} \cdot g_{\boldsymbol{\lambda}(\ell),\boldsymbol{\theta}}(x,y), \tag{8}$$

where $\alpha_{\boldsymbol{\lambda}(\ell)}^{c}$ represents the multiplicative factor between the holographic data recorded on channel c and the model generated at the wavelength $\boldsymbol{\lambda}(\ell)$, and m_0^{c*} is the offset that results from the mixing offsets m_0^R, m_0^G and m_0^B.

The signal ratio $q_{\boldsymbol{\lambda}(\ell)}^{c}$ produced by an illumination at wavelength $\boldsymbol{\lambda}(\ell)$ and which is actually recorded on sensor channel c due to the spectral crosstalk effect can be estimated by the ratio given by

$$q_{\boldsymbol{\lambda}(\ell)}^{c} = \frac{\alpha_{\boldsymbol{\lambda}(\ell)}^{c}}{\sum_{c\in\{R,G,B\}} \alpha_{\boldsymbol{\lambda}(\ell)}^{c}} \Rightarrow Q = \begin{pmatrix} q_R^R & q_R^G & q_R^B \\ q_G^R & q_G^G & q_G^B \\ q_B^R & q_B^G & q_B^B \end{pmatrix}. \tag{9}$$

Thus, the mixing matrix Q characterizes the crosstalk effect. Its nine mixing coefficients, $q_{\boldsymbol{\lambda}(\ell)}^{c}$, are obtained by recording the three color holograms produced by the illumination of a parametric object at the three available wavelengths. For each of these three holograms, reconstructions have to be carried out for each of the three hologram channels using a parametric model for each wavelength. The multiplicative factors $\alpha_{\boldsymbol{\lambda}(\ell)}^{c}$ correspond to the correlation coefficient between data recorded on channel c illuminated by wavelength $\boldsymbol{\lambda}(\ell)$ and the model at this same wavelength. The principle of the crosstalk calibration method is illustrated in Fig. 5 for wavelength λ_R. A non-zero signal is visible on the three color channels, thereby proving the presence of crosstalk. As detailed in Section 2, the crosstalk phenomenon cannot be accurately estimated by an average of the intensities received on each channel due to the nonlinearity of the camera response and the non-uniform background varying over time. The proposed calibration method takes advantage of the modulation of the recorded signal induced by the holographic object to accurately estimate this phenomenon.

2. Experimental Results and Discussion

Table 4 shows the estimated mean and standard deviation (related to the standard deviation of the estimated parameters $\boldsymbol{\theta}$) of the crosstalk mixing matrix Q_{exp} obtained from the 65 sets of three holograms recorded at the respective wavelengths $\{\lambda_R^{\text{real}}, \lambda_G^{\text{real}}, \lambda_B^{\text{real}}\}$. Table 5 shows the Q_m mixing matrix values extracted from the data provided by the manufacturer.

Using this scheme, it appears that the estimated mixing coefficients are very close to those deduced from the

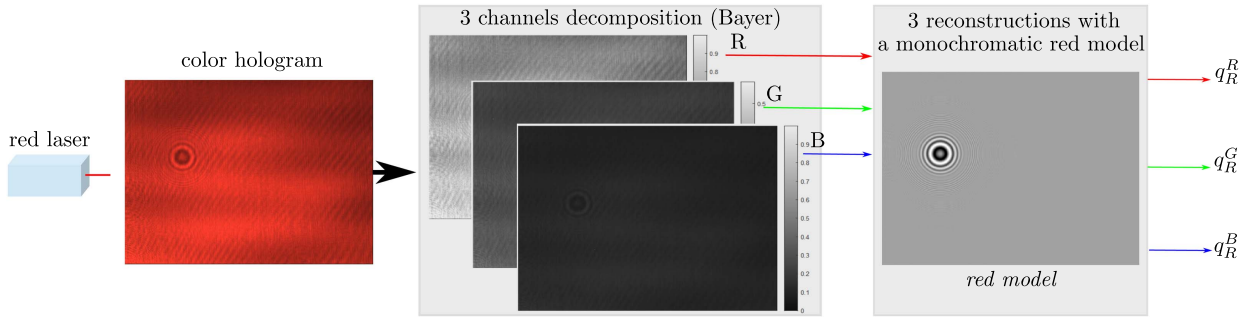

Fig. 5. Parametric estimation principle of channel mixing coefficients induced by the crosstalk phenomenon.

manufacturer's spectral responses of the Bayer filters. This indicates that the crosstalk effect of our camera is mainly due to the spectral crosstalk (the electronic crosstalk effect being negligible). Thus, it appears that for each channel, approximately 25% of the signal of interest is transferred to the two other channels due to the crosstalk effect. This observation suggests that it is important to take this phenomenon into account in the holographic model used during the reconstruction step. Note that, in practice, only one set of holograms is needed to obtain a spectral crosstalk estimation (whose standard deviation is given in Table 4). The application of this method to another camera of the same make led to a crosstalk matrix close to the one obtained here. Minor variations can be attributed to the camera's variability (e.g., homogeneity of the filters, local orientation of the microlenses, etc.). However, in the following paragraph, it will be emphasized that it is beneficial to estimate the mixing matrix Q more accurately than by just reading the values provided by the manufacturer. Indeed, a significant discrepancy was observed for the blue light intensity distribution on the different channels between the estimated values and the values derived from the manufacturer's datasheets.

3. Accounting for Crosstalk in the Parametric Model

Here we focus on accounting for the effects of spectral crosstalk in the holographic model used for hologram reconstruction (see Section 3). For that purpose, vector $\boldsymbol{g}$ containing the holographic models on the different channels c is replaced with $\boldsymbol{g}^*$ according to

$$\boldsymbol{g}^*(x,y) = \begin{pmatrix} g^{*R}_{\lambda,\boldsymbol{\theta}}(x,y) \\ g^{*G}_{\lambda,\boldsymbol{\theta}}(x,y) \\ g^{*B}_{\lambda,\boldsymbol{\theta}}(x,y) \end{pmatrix} = Q^T \cdot \begin{pmatrix} g_{\lambda_R,\boldsymbol{\theta}}(x,y) \\ g_{\lambda_G,\boldsymbol{\theta}}(x,y) \\ g_{\lambda_B,\boldsymbol{\theta}}(x,y) \end{pmatrix} = Q^T.\boldsymbol{g}(x,y), \quad (10)$$

in which Q^T stands for the transposed of matrix Q. This equation expresses the mixture of signals from the different sources on each channel c. Figure 6 illustrates this principle. Rather than separating the signals received on each sensor channel (by unmixing), this method mixes the hologram formation model in the same way as the recorded data.

We have applied the proposed crosstalk correction method on a set of 65 color holograms ($z_p \simeq 7$ cm, $r_p = 15$ µm, with random transversal shifts at most a few pixels). Since the exact optical magnification of the setup is not precisely known, the absolute estimation bias cannot be obtained for real holograms. Thus, the quality of the reconstruction is evaluated based on the normalized correlation coefficient between the hologram formation model and the recorded data. We observed that taking the spectral crosstalk into account results on average in an improvement of the normalized correlation coefficient by 1.5%.

Table 4. Estimated Crosstalk Mixing Matrix Q_{exp} (in Percent)

	C^R	C^G	C^B
λ_R	74.9 ± 0.1	15.4 ± 0.1	9.7 ± 0.1
λ_G	11.7 ± 0.1	72.4 ± 0.2	15.9 ± 0.2
λ_B	14.0 ± 0.1	11.1 ± 0.1	74.9 ± 0.1

Table 5. Manufacturer's Spectral Crosstalk Mixing Matrix Q_m (in Percent), Deduced from Basler, daA2500-14uc Documentation

	C^R	C^G	C^B
λ_R	74	16	10
λ_G	12	70	18
λ_B	14	14	72

4. Influence of z_p and r_p on the Quality of the Reconstruction

In order to evaluate the influence of z_p and r_p on the quality of the reconstruction using the proposed crosstalk correction method, we have carried out numerical simulations of holograms for different sets of parameters z_p ($z_p \in [7\text{ cm}; 12\text{ cm}]$) and r_p ($r_p \in [15\text{ µm}; 50\text{ µm}]$). For each pair of values $\{z_p, r_p\}$, 100 color holograms [Eq. (8)] located in the center of the field of view are generated with an additive white and Gaussian noise and a signal-to-noise ratio (SNR) equal to 2.5.

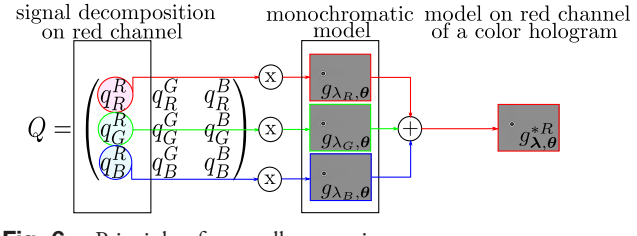

Fig. 6. Principle of crosstalk correction.

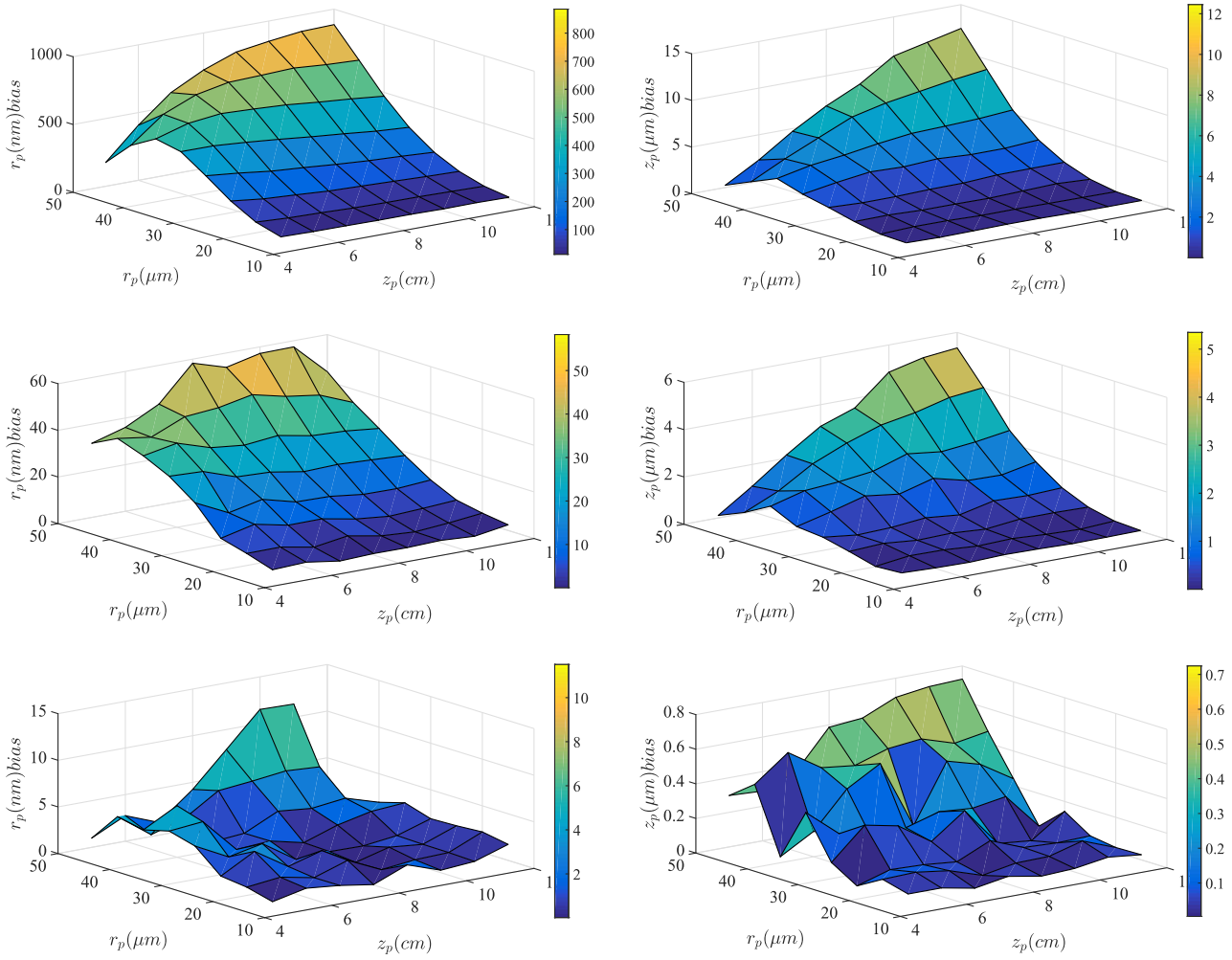

Fig. 7. Bias on estimated r_p (left) and z_p (right) without crosstalk correction (first line), with crosstalk correction using Q_m (second line) and with crosstalk correction using Q_{exp} (third line) for a centered object with radius $r_p \in [15\ \mu\text{m}; 50\ \mu\text{m}]$ located at $z_p \in [7\ \text{cm}; 12\ \text{cm}]$ from the sensor plane.

Figure 7 shows the reconstruction bias on the estimated parameters z_p and r_p. Table 6 corresponds to one of the configurations illustrated in Fig. 7.

Table 6 shows that taking the crosstalk into account in the hologram formation model reduces the estimation bias by a factor between 3 (using Q_m) and 5 (using Q_{exp}) for the estimated z_p parameter and by a factor between 20 (using Q_m) and 70 (using Q_{exp}) for the estimated r_p parameter for an object whose radius is 15 μm and located at 7 cm from the sensor plane. Correction by an approximate crosstalk matrix enables a significant reduction in estimation bias. This bias is further reduced when the crosstalk matrix used in the reconstruction step is closer to that generating the channel mixing. This justifies the use of an accurate estimation of spectral crosstalk. It should be noted that the standard deviation is not reduced by taking the spectral crosstalk into account. Indeed it is dependent on the SNR and the estimation method. In addition, since a change of the z_p and r_p parameters causes a frequency modification in the hologram signal, the crosstalk phenomenon can generate a more or less important frequency mixing according to the experimental parameters. As a result, the estimation of these parameters without crosstalk correction generates a bias depending on the importance of the frequency mixing (especially important when z_p and r_p increase simultaneously, as shown in Fig. 7). This shows that reconstructions without accounting for crosstalk cannot be easily compensated for the bias since the bias is not constant.

Table 6. Bias and Standard Deviation on Estimated Parameters z_p and r_p Without Crosstalk Correction (First Line), With Crosstalk Correction Using Q_m (Second Line) and With Crosstalk Correction Using Q_{exp} (Third Line) for a Centered Object with Radius $r_p = 15\ \mu$m Located at $z_p = 7$ cm from the Sensor Plane

	Bias on z_p (nm)	Std. Dev. on z_p (nm)	Bias on r_p (nm)	Std. Dev. on r_p (nm)
Without correction	52	316.3	21	5.0
With crosstalk correction (Q_m)	15	315.5	0.50	4.8
With crosstalk correction (Q_{exp})	9.9	315.5	0.28	4.8

5. THEORETICAL LIMITS OF PRECISION

In this section, we discuss the theoretical limits of precision reachable on the estimated parameters $\boldsymbol{\theta} = \{x_p, y_p, z_p, r_p\}$ in a monochromatic and color hologram recording framework. The aim is to investigate whether the consideration of a mosaicked color hologram, which can be impacted by the crosstalk phenomenon, provides at least equal performances to those obtained with a monochromatic hologram.

The minimum achievable resolution on the estimated parameters can be statistically evaluated using the Cramèr–Rao lower bounds (CRLBs). The variance of any unbiased estimator is bounded from below by the CRLBs, which are obtained from the diagonal of the inverse Fisher information matrix [46]. As a result, these limits represent the minimum estimate variance theoretically achievable when the noise is additive white and Gaussian. CRLBs constitute only a theoretical tool useful for relative comparison between different experimental configurations. By describing the light intensity recorded on the sensor by the direct model [Eq. (4)] and by performing a statistical analysis on the estimated parameters for a given noise variance, it is possible to obtain the theoretical standard deviation δ_p for each estimated parameter $p \in \boldsymbol{\theta}$. This method, which was applied to digital holography in [47], is applied here to color holograms in taking into account the possible mixture of the color signals due to a crosstalk phenomenon. Equation (11) gives the Fisher information matrix I depending on the model gradients, the amplitude factor of the model α and the variance σ_b^2 of the noise. Equation (12) gives the link between the CRLBs and matrix I. When crosstalk signal mixing occurs, the color model vector $\boldsymbol{g}$ is replaced with $\boldsymbol{g}^*$ according to Eq. (10):

$$[I(\boldsymbol{\theta})]_{i,j} = \frac{\alpha^2}{\sigma_b^2} \cdot \sum_{a=1}^{A} \sum_{b=1}^{B} \left(\frac{\partial \boldsymbol{g}_{\boldsymbol{\theta}}(a,b).\boldsymbol{w}(a,b)}{\partial \theta_i} \right) \cdot \left(\frac{\partial \boldsymbol{g}_{\boldsymbol{\theta}}(a,b).\boldsymbol{w}(a,b)}{\partial \theta_j} \right), \tag{11}$$

$$\delta_i = \sqrt{[I(\boldsymbol{\theta})^{-1}]_{i,i}}. \tag{12}$$

The theoretical limits of precision are obtained by considering a hologram model of a particle of radius $r_p = 15$ μm located at a distance of $z_p = 7$ cm with an SNR equal to 2.5. Table 7 shows the reachable theoretical resolutions according to each parameter $p \in \boldsymbol{\theta}$. This study was performed in the following six cases:

- A monochromatic hologram obtained with only one source and recorded by a monochromatic sensor (cases 1, 2 and 3, respectively, denoted by λ_R, λ_G and λ_B in Table 7 and Fig. 8).
- A trichromatic hologram artificially formed by the concatenation of three holograms recorded by a monochromatic sensor without mosaicking as in [48,49] (case 4 denoted by $\lambda_{R,G,B}$).
- A mosaicked color hologram recorded by a Bayer color sensor not affected by the crosstalk phenomenon (case 5 denoted by $\lambda_{R,G,B}$ + Bayer).
- A mosaicked color hologram recorded by a Bayer color sensor affected by the crosstalk phenomenon defined by the mixing matrix Q_{exp} estimated from the experimental holograms (case 6 denoted by $\lambda_{R,G,B}$ + Bayer + ct).

Table 7. CRLBs for the Reconstructed Parameters

	δ_x (nm)	δ_y (nm)	δ_z (nm)	δ_r (nm)
λ_R	0.56	0.49	31	0.37
λ_G	0.59	0.55	35	0.40
λ_B	0.70	0.63	41	0.46
$\lambda_{R,G,B}$	0.32	0.35	20	0.13
$\lambda_{R,G,B}$ + Bayer	0.53	0.50	31	0.22
$\lambda_{R,G,B}$ + Bayer + ct	0.70	0.80	40	0.30

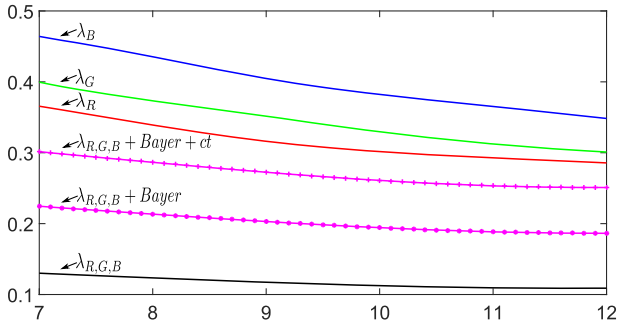

Fig. 8. CRLBs on particle radius for different distances between the sensor and object.

The mean results may vary slightly depending on the position of the particle in the sensor field. Figure 8 completes this study by showing the evolution of the achievable precision limits for a distance between the sensor and object varying from 7 cm to 12 cm in the same cases as those listed Table 7.

It appears that color holograms that undergo mosaicking during the acquisition step suffer from an increase in CRLBs (and, hence, a degradation in the reconstruction) with respect to a color hologram artificially formed by the concatenation of three monochromatic holograms (obtained with the three available wavelengths in our experimental setup). This is explained by the fact that the mosaicking step results in a reduction by a factor of 3 in the number of pixels recorded, resulting in lost information. It also appears that holograms not tainted by a crosstalk phenomenon lead to finer resolutions than holograms tainted by this effect. This can be explained by the blurring of high frequencies due to mixing of the color signals when spectral crosstalk occurs. This observation justifies why the spectral crosstalk phenomenon that occurs with most color sensors equipped with a Bayer filter has an influence in metrological application using an in-line holographic setup. Finally, we observed that it is possible to obtain a finer precision of the r_p parameter by considering a color hologram, due to additional information provided by wavelength diversity.

6. CONCLUSION

In lensless color microscopy, calibration of the wavelength of the sources and of the crosstalk phenomenon caused by Bayer filters is important for quantitative imaging. We showed that inaccurate estimation of wavelengths or crosstalk leads to inaccurate reconstructions. We proposed an experimental self-calibration process based on an inverse problem reconstruction

and studied its performance. This self-calibration is simple to apply since it only requires the lensless color microscopy setup. Any spherical object whose diffraction pattern can be described by a direct model (Thompson model [42] for an opaque object or [Generalized] Lorenz–Mie model [50,51] for droplets, bubble or beads) can be used. For estimation of laser diode wavelengths, the suggested method makes it possible to accurately estimate two wavelengths based on the value of the third taken as a reference. Considering the wavelength with the smallest uncertainty range provided by the manufacturer as a reference, we demonstrate that it is possible to obtain uncertainty ranges for the two other wavelengths that are narrower than the typical ranges provided by the manufacturer. The uncertainty on the estimated wavelengths is reduced considerably if the uncertainty on the reference wavelength is small. Work is now underway to jointly estimate the three wavelengths using a set of several color holograms recorded at different distances between the sensor and object, and to also estimate the widths of the spectral sources by taking them into account in the hologram formation model.

In the same way, we also proposed an experimental method using an inverse parametric approach to estimate the spectral crosstalk phenomenon that occurs on a color sensor equipped with a Bayer filter and which results in a mixing of the channels. It has been shown that after having estimated this phenomenon, it is possible to take it into account to reduce estimation bias or to increase the correlation between the recorded data and the hologram formation model.

Finally, it has been shown that the color holograms acquired with a Bayer color sensor suffer from a degradation of the theoretical limits of estimation precision with respect to a trichromatic color image that does not undergo mosaicking. Similarly, the presence of crosstalk leads to an additional degradation of the theoretical limits of precision due to the blurring introduced by mixing of different color signals. However, the theoretical limit on the estimated radius of the holographic object is improved with respect to a monochromatic acquisition, thanks to wavelength diversity. The methods for estimating wavelengths and crosstalk lead to calibration parameters that can be used whatever the final reconstruction method is.

Funding. Agence Nationale de la Recherche (ANR) (ANR-11-IDEX-0007, ANR-11-LABX-0063); DETECTION-CNRS DEFI IMAGIn 2015.

REFERENCES

1. L. Repetto, E. Piano, and C. Pontiggia, "Lensless digital holographic microscope with light-emitting diode illumination," Opt. Lett. **29**, 1132–1134 (2004).
2. J. Garcia-Sucerquia, W. Xu, S. K. Jericho, P. Klages, M. H. Jericho, and H. J. Kreuzer, "Digital in-line holographic microscopy," Appl. Opt. **45**, 836–850 (2006).
3. J. Katz and J. Sheng, "Applications of holography in fluid mechanics and particle dynamics," Annu. Rev. Fluid Mech. **42**, 531–555 (2010).
4. K. D. Hinsch, "Holographic particle image velocimetry," Meas. Sci. Technol. **13**, R61 (2002).
5. O. Mudanyali, E. McLeod, W. Luo, A. Greenbaum, A. F. Coskun, Y. Hennequin, C. P. Allier, and A. Ozcan, "Wide-field optical detection of nanoparticles using on-chip microscopy and self-assembled nanolenses," Nat. Photonics **7**, 240–247 (2013).
6. C. Allier, G. Hiernard, V. Poher, and J. Dinten, "Bacteria detection with thin wetting film lensless imaging," Biomed. Opt. Express **1**, 762–770 (2010).
7. L. Denis, C. Fournier, T. Fournel, and C. Ducottet, "Numerical suppression of the twin image in in-line holography of a volume of micro-objects," Meas. Sci. Technol. **19**, 074004 (2008).
8. J. Gire, L. Denis, C. Fournier, É. Thiébaut, F. Soulez, and C. Ducottet, "Digital holography of particles: benefits of the 'inverse problem' approach," Meas. Sci. Technol. **19**, 074005 (2008).
9. S. N. A. Morel, A. Delon, P. Blandin, T. Bordy, O. Cioni, L. Hervé, C. Fromentin, J.-M. Dinten, and C. Allier, "Wide-field lensfree imaging of tissue slides," in *Advanced Microscopy Techniques IV; and Neurophotonics II* (Optical Society of America, 2015), paper 95360K.
10. D. Gabor, "A new microscope principle," Nature **161**, 777–778 (1948).
11. H. Royer, "An application of high-speed microholography: the metrology of fogs," Nouv. Rev. Opt. **5**, 87–93 (1974).
12. J. W. Goodman, *Introduction to Fourier Optics* (Roberts & Company, 2005).
13. U. Schnars and W. P. Jüptner, "Digital recording and numerical reconstruction of holograms," Meas. Sci. Technol. **13**, R85–R101 (2002).
14. F. Soulez, L. Denis, C. Fournier, É. Thiébaut, and C. Goepfert, "Inverse-problem approach for particle digital holography: accurate location based on local optimization," J. Opt. Soc. Am. A **24**, 1164–1171 (2007).
15. C. Fournier, L. Denis, E. Thiebaut, T. Fournel, and M. Seifi, "Inverse problem approaches for digital hologram reconstruction," Proc. SPIE **8043**, 80430S (2011).
16. L. Denis, D. Lorenz, E. Thiébaut, C. Fournier, and D. Trede, "Inline hologram reconstruction with sparsity constraints," Opt. Lett. **34**, 3475–3477 (2009).
17. C. Fournier, F. Jolivet, L. Denis, N. Verrier, E. Thiébaut, C. Allier, and T. Fournel, "Pixel super-resolution in digital holography by regularized reconstruction," Appl. Opt. **56**, 69–77 (2017).
18. J. Garcia-Sucerquia, "Color digital lensless holographic microscopy: laser versus led illumination," Appl. Opt. **55**, 6649–6655 (2016).
19. W. Li, P. Ogunbona, Y. Shi, and I. Kharitonenko, "Modelling of color cross-talk in CMOS image sensors," in *IEEE International Conference on Acoustics, Speech, and Signal Processing (ICASSP)* (IEEE, 2002), Vol. **4**, pp. IV-3576–IV-3579.
20. L. Blockstein and O. Yadid-Pecht, "Crosstalk quantification, analysis, and trends in CMOS image sensors," Appl. Opt. **49**, 4483–4488 (2010).
21. A. Getman, T. Uvarov, Y. Han, B. Kim, J. Ahn, and Y. Lee, "Crosstalk, color tint and shading correction for small pixel size image sensor," in *International Image Sensor Workshop* (2007), pp. 166–169.
22. P. Tankam, P. Picart, D. Mounier, J. M. Desse, and J.-C. Li, "Method of digital holographic recording and reconstruction using a stacked color image sensor," Appl. Opt. **49**, 320–328 (2010).
23. P. M. Hubel, J. Liu, and R. J. Guttosch, "Spatial frequency response of color image sensors: Bayer color filters and Foveon x3," Proc. SPIE **5301**, 402–407 (2004).
24. B. E. Bayer, "Color imaging array," U.S. patent 3, 971, 065 (20 July 1976).
25. Z. Göröcs, L. Orzó, M. Kiss, V. Tóth, and S. Tökés, "In-line color digital holographic microscope for water quality measurements," Proc. SPIE **7376**, 737614 (2010).
26. I. Yamaguchi, T. Matsumura, and J.-I. Kato, "Phase-shifting color digital holography," Opt. Lett. **27**, 1108–1110 (2002).
27. Y. Wu, Y. Zhang, W. Luo, and A. Ozcan, "Demosaiced pixel super-resolution for multiplexed holographic color imaging," Sci. Rep. **6**, 28601 (2016).
28. K. Hirakawa and P. J. Wolfe, "Spatio-spectral color filter array design for enhanced image fidelity," in *IEEE International Conference on Image Processing (ICIP)* (IEEE, 2007), Vol. **2**, pp. II-81–II-84.
29. L. Anzagira and E. R. Fossum, "Color filter array patterns for small-pixel image sensors with substantial cross talk," J. Opt. Soc. Am. A **32**, 28–34 (2015).

30. Y. Yu, Q. Chen, L. Wen, X. Hu, and H.-F. Zhang, "Spatial optical crosstalk in CMOS image sensors integrated with plasmonic color filters," Opt. Express **23**, 21994–22003 (2015).
31. Q. Chen and D. R. Cumming, "High transmission and low color crosstalk plasmonic color filters using triangular-lattice hole arrays in aluminum films," Opt. Express **18**, 14056–14062 (2010).
32. S. Yokogawa, S. P. Burgos, and H. A. Atwater, "Plasmonic color filters for CMOS image sensor applications," Nano Lett. **12**, 4349–4354 (2012).
33. G. Agranov, V. Berezin, and R. H. Tsai, "Crosstalk and microlens study in a color CMOS image sensor," IEEE Trans. Electron Dev. **50**, 4–11 (2003).
34. M. Furumiya, H. Ohkubo, Y. Muramatsu, S. Kurosawa, F. Okamoto, Y. Fujimoto, and Y. Nakashiba, "High-sensitivity and no-crosstalk pixel technology for embedded CMOS image sensor," IEEE Trans. Electron Dev. **48**, 2221–2227 (2001).
35. M. Estribeau and P. Magnan, "CMOS pixels crosstalk mapping and its influence on measurements accuracy for space applications," Proc. SPIE **5978**, 597813 (2005).
36. C.-H. Koo, H.-K. Kim, K.-H. Paik, D.-C. Park, K.-H. Lee, Y.-K. Park, C.-R. Moon, S.-H. Lee, S.-H. Hwang, D.-H. Lee, and J.-T. Kong, "Improvement of crosstalk on 5 m CMOS image sensor with 1.7 × 1.7 μm^2 pixels," Proc. SPIE **6471**, 647115 (2007).
37. T.-H. Hsu, Y.-K. Fang, C. Lin, S. Chen, C. Lin, D.-N. Yaung, S.-G. Wuu, H. Chien, C. Tseng, J. Lin, and C. S. Wang, "Light guide for pixel crosstalk improvement in deep submicron CMOS image sensor," IEEE Electron. Dev. Lett. **25**, 22–24 (2004).
38. S.-H. Lee, Y. Roichman, G.-R. Yi, S.-H. Kim, S.-M. Yang, A. Van Blaaderen, P. Van Oostrum, and D. G. Grier, "Characterizing and tracking single colloidal particles with video holographic microscopy," Opt. Express **15**, 18275–18282 (2007).
39. M. Seifi, C. Fournier, N. Grosjean, L. Méès, J.-L. Marié, and L. Denis, "Accurate 3D tracking and size measurement of evaporating droplets using in-line digital holography and "inverse problems" reconstruction approach," Opt. Express **21**, 27964–27980 (2013).
40. N. Verrier, N. Grosjean, E. Dib, L. Méès, C. Fournier, and J. Marié, "Improvement of the size estimation of 3D tracked droplets using digital in-line holography with joint estimation reconstruction," Meas. Sci. Technol. **27**, 045001 (2016).
41. N. Verrier, C. Fournier, L. Méès, and T. Fournel, "In-line particle holography with an astigmatic beam: setup self-calibration using an "inverse problems" approach," Appl. Opt. **53**, G147–G156 (2014).
42. G. A. Tyler and B. J. Thompson, "Fraunhofer holography applied to particle size analysis a reassessment," J. Mod. Opt. **23**, 685–700 (1976).
43. C. Fournier, L. Denis, M. Seifi, and T. Fournel, *Digital Hologram Processing in On-Axis Holography, in Multi-Dimensional Imaging*, B. Javidi, E. Tajahuerce, and P. Andrés, eds. (Wiley, 2014).
44. F. Nicolas, S. Coetmellec, M. Brunel, and D. Lebrun, "Digital in-line holography with a sub-picosecond laser beam," Opt. Commun. **268**, 27–33 (2006).
45. F. Nicolas, S. Coëtmellec, M. Brunel, and D. Lebrun, "Suppression of the moiré effect in sub-picosecond digital in-line holography," Opt. Express **15**, 887–895 (2007).
46. A. Stuart and J. Odd, *Kendall's Advanced Theory of Statistics: Distribution Theory* (Arnold, 1994).
47. C. Fournier, L. Denis, and T. Fournel, "On the single point resolution of on-axis digital holography," J. Opt. Soc. Am. A **27**, 1856–1862 (2010).
48. J. Zhao, H. Jiang, and J. Di, "Recording and reconstruction of a color holographic image by using digital lensless Fourier transform holography," Opt. Express **16**, 2514–2519 (2008).
49. N. Demoli, D. Vukicevic, and M. Torzynski, "Dynamic digital holographic interferometry with three wavelengths," Opt. Express **11**, 767–774 (2003).
50. G. Mie, "Beiträge zur optik trüber medien, speziell kolloidaler metallösungen," Ann. Phys. **330**, 377–445 (1908).
51. L. Méès, N. Grosjean, D. Chareyron, J.-L. Marié, M. Seifi, and C. Fournier, "Evaporating droplet hologram simulation for digital in-line holography setup with divergent beam," J. Opt. Soc. Am. A **30**, 2021–2028 (2013).